ACS Catalysis

Research Article

pubs.acs.org/acscatalysis

Effects of Surface and Bulk Silver on $PrMnO_{3+\delta}$ Perovskite for CO and Soot Oxidation: Experimental Evidence for the Chemical State of Silver

Suresh Kumar Megarajan,[†] Sadhana Rayalu,[†] Maiko Nishibori,[‡] Yasutake Teraoka,[‡] and Nitin Labhsetwar*,[†]

[†]Environmental Materials Division, CSIR–National Environmental Engineering Research Institute (CSIR-NEERI), Nehru Marg, Nagpur, 440020 India

[‡]Department of Energy and Material Sciences, Faculty of Engineering Sciences, Kyushu University, Kasuga, Fukuoka 816-8580, Japan

Supporting Information

ABSTRACT: Unambiguous evidence has been obtained to explain the presence and effects of both framework and extra-framework silver on catalytic properties of $Pr(Ag)MnO_{3+\delta}$ perovskite type materials, using various tools such as XPS, HR-TEM, O_2-TPD, and H_2-TPR analysis. Three types of Ag-incorporated $PrMnO_3$ perovskite samples were synthesized by means of Ag partial substitution in perovskite lattice and Ag dispersion on the surface of the synthesized perovskite phase, using two different calcination temperatures of 200 and 550 °C. The amount of silver used was 1 wt % (0.000225 mol), in all three catalysts. On the basis of extensive characterization studies, it was clearly explained that the partially substituted Ag for Pr is present in the lattice along with Pr at the "A" site of the ABO_3 perovskite structure. The Ag surface incorporated $PrMnO_{3+\delta}$ sample calcined at 550 °C shows both surface metallic silver and partially substituted Ag in perovskite lattice, whereas Ag_2O nanoparticles were observed on the surface in the case of another sample calcined at 200 °C. All of the synthesized materials were evaluated for their CO and soot oxidation activity, considering the renewed interest in Ag promoted catalytic materials and ambiguity about its location in the perovskite structure as well as its role in promoting catalytic and other properties of perovskite type materials. Perovskites with surface Ag species show better catalytic activity than the Ag substituted counterpart. This improved and better activity of Ag dispersed samples was because of the presence of the surface active redox couple of Ag/Ag_2O, which facilitates the surface redox reaction pathway of CO and soot oxidation reactions.

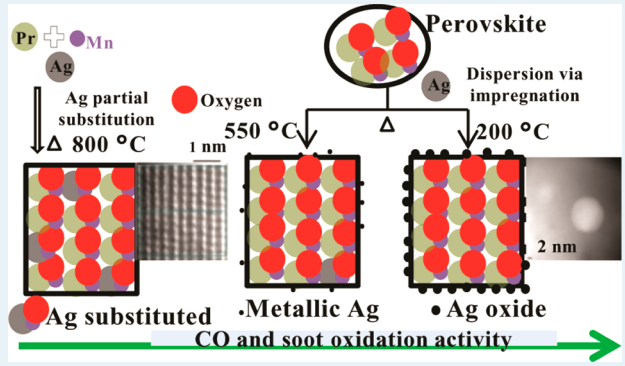

KEYWORDS: *perovskite, $PrMnO_{3+\delta}$, silver, catalysis, CO oxidation*

INTRODUCTION

Perovskite type materials have been considered as potential candidates for diversified applications, such as high-temperature superconductivity, magnetoresistance, ionic conductivity, dielectric properties, sensors, solid-oxide fuel cells (SOFC), membrane separation, catalysis, and many other areas.[1−7] In the field of heterogeneous catalysis, perovskites are well-explored materials for CO and hydrocarbon oxidation as well as de-NOx reactions and are often considered as potential substitutes for noble metal based three-way and soot oxidation catalysts. Catalysts with better chemical and thermal stability as well as lower cost are usually preferred for industrial applications. Perovskites are promising catalytic materials due to their low cost and thermal stability and recently started getting more attention due to their enhanced chemical stability in lowering fuel sulfur. Perovskites are generally prepared by following high-temperature calcination, which often results in sintered phases with low surface area. The general chemical formula of perovskites is ABO_3, in which A ions can be rare earth, alkaline earth, and other large ions, whereas B ions are often first-row transition metal ions. In this ABO_3 structure, often the coordination number of the A cation is 12, whereas the coordination number of the B cation is generally 6.[8−11] Their catalytic activity almost exclusively depends on the B site cation; however, the A site cation can also influence the overall catalytic activity of a catalyst, primarily by affecting the oxidation states of the B site cation and thereby changing the overall redox properties of the perovskite phase.

Precious metal promoted/substituted perovskite type catalytic materials are being increasingly explored and considered as promising substitutes for platinum, palladium, and rhodium in three-way catalysis and other catalytic applications.[12−18] Over

Received: June 21, 2014
Revised: September 28, 2014
Published: November 7, 2014

the past few years, however, silver-based perovskites governed a large attraction toward various catalysis research because of their lower cost compared to their precious metal counterparts. Wang et al. reported Ag-modified $La_{0.6}Sr_{0.4}MnO_3$ catalyst for complete oxidation of methanol and ethanol. They also compared the activity with Pt and Pd supported alumina catalysts. They found that the Ag-modified perovskite shows better activity than precious metal supported catalysts and concluded that improved redox properties of Ag-modified perovskite are the most important reason to get enhanced catalytic activity rather than noble metal counterparts.[19] Series of silver-doped $La_{0.6}Ce_{0.4}CoO_3$ perovskite catalysts were studied for the reduction of nitrogen monoxide with propane in the presence of oxygen by Liu et al. They observed that improved NO reduction is mainly due to the partially substituted silver ions, which were indeed doped onto the surface of perovskite. This partial substitution of Ag in perovskite lattice occurs mainly because of the similar ionic radii of La and Ag and is responsible for the improved redox properties and better catalytic activity.[20] Choudhary et al. studied Ag-doped perovskites for methane combustion and observed partially substituted silver significantly increases the catalytic activity of perovskite catalyst at low temperature even at very high space velocity.[21] Kucharczyk et al. studied a series of monolithic $La_{1-x}Ag_xMnO_3$ perovskites for CH_4 combustion and CO oxidation, respectively. They reported that a significant enhancement in CO oxidation was observed for $LaMnO_3$ if the silver substitution was ≥10 mol % (i.e., $x \geq 0.1$). It was concluded that the higher activity of the Ag-substituted catalyst is mainly due to the presence of silver oxide phase and the high Mn^{4+}/Mn^{3+} ratio on the perovskite surface.[22] A set of Ag-doped $LaCoO_3$ perovskites were synthesized by different methods and reported for flameless methane combustion by Buchneva et al. They observed the influence of various factors on catalytic activity, such as synthesis methods, amount of Ag doped, doping methods, and the particle size of extra-framework silver.[23] Buchneva et al. have also synthesized various Ag-dispersed as well as -substituted $LaMnO_3$ perovskites by using different methods and reported their activity for flameless methane combustion. They have observed an increase in the activity of $LaMnO_3$ for CH_4 oxidation, when Ag was substituted into the lattice structure of perovskite.[24] Pecchi et al. synthesized $La_{1-x}Ag_xMn_{0.9}Co_{0.1}O_3$ (x_{Ag} = 0.0, 0.1, 0.2, 0.3) catalysts and reported catalytic removal of *n*-hexane. They observed complete partial substitution for 10 mol % of Ag, whereas a segregated silver phase along with lattice Ag was observed in the case of partial substitution beyond 10 mol %.[25]

From the literature, hence, it is known that silver-based perovskite systems are among the potential candidates for various catalytic applications. Although there are number of papers on silver-containing perovskites, comprehensive structural characterization to investigate the state of silver in perovskites is still one of the major challenges and needs more work to unambiguously establish the mechanistic aspects. The major puzzle in silver-substituted perovskite is the location of Ag. Is it present in the lattice structure or on the surface of perovskite? The dilemma is the same for surface-doped/dispersed Ag perovskite system considering the mobility of Ag. Moreover, most of the papers are also on perovskites containing higher amounts of Ag, and none of these studies have reported the same Ag loading for both partial substitution and surface dispersion, respectively, which further makes things complicated to compare and interpret. The detailed characterization was also the major limitation to prove the structural properties as well as redox properties of Ag-substituted perovskites.

With this background, the main objective of this research work is to study the structural as well as redox properties of Ag-substituted/dispersed perovskites and to unambiguously establish the state and location of Ag in perovskite type structure. The present study was focused on the synthesis, detailed characterization, and catalytic studies of $PrMnO_{3+\delta}$ perovskite, partially substituted $PrMnO_{3+\delta}$ by Ag at the A site, and various Ag-dispersed $PrMnO_{3+\delta}$ (in which Ag is expected on the surface) toward CO and soot oxidation reactions. In the case of both Ag-substituted and Ag surface dispersed perovskites, it was possible to study the presence and state of silver using TEM analysis with an atomic mapping facility. O_2-TPD (temperature-programmed desorption) and H_2-TPR (temperature-programmed reduction) analyses were carried out to study the redox properties of these different Ag-incorporated perovskites. XPS studies were also carried out to explain the oxidation state of Ag in perovskites, and they could reveal the change in redox properties as a function of the presence of silver in the perovskite structure or on the perovskite surface.

EXPERIMENTAL SECTION

Material Preparation. Laboratory grade praseodymium nitrate (Acros-India Ltd.), manganese nitrate (Merck-India Ltd.), silver nitrate (Merck-India Ltd.), and citric acid (Merck-India Ltd.) were used directly without further purification. $PrMnO_{3+\delta}$ catalyst was prepared by following the citrate method. An aqueous solution of praseodymium nitrate (0.01 mol), manganese nitrate (0.01 mol), and citric acid (0.03 mol) was prepared using the requisite amount of water and mixed by vigorous stirring. The mixed metal and citric acid solution was heated at 110 °C until the water was evaporated. The spongy material thus obtained was homogenized by grinding, and it was further calcined at 800 °C for 8 h in a muffle furnace and denoted PM. The above synthesis procedure was also used to prepare $Pr_{0.9775}Ag_{0.0225}MnO_{3+\delta}$ (denoted PAM) by using praseodymium nitrate (0.009775 mol), silver nitrate (0.000225 mol), manganese nitrate (0.01 mol), and citric acid (0.03 mol). One weight percent $Ag/PrMnO_{3+\delta}$ (Ag = 0.000225 mol) samples were prepared by means of the conventional impregnation method and calcined at two different temperatures. The calcined PM powder was soaked with aqueous $AgNO_3$ solution and dried at 80 °C with homogenization. The sample thus obtained was calcined separately at 200 and 550 °C for 5 h and denoted APM-200 and APM-550, respectively.

Physicochemical Characterization. All of the synthesized catalysts have been characterized by X-ray powder diffraction by using an Ultima (Rigaku, Japan) machine operated at 40 kV and 40 mA with a monochromator using Cu Kα radiation. The samples were scanned in the 2θ range 10−90° with a scanning speed of 5°/min. Diffraction peaks were compared with the standard database reported by the Joint Committee on Powder Diffraction Standards (JCPDS). Crystallite size was calculated using Sherrer's equation.

The specific surface area (Brunauer−Emmett−Teller method) of samples was analyzed by following the standard nitrogen method using a BEL-SORP mini instrument (BEL Japan). The samples were previously evacuated and pretreated at 200 °C for 2 h in a helium atmosphere.

dx.doi.org/10.1021/cs500880w | ACS Catal. 2015, 5, 301−309

The morphological and structural details of the materials were studied by field emission scanning electron microscopy (FE-SEM) and high-resolution transmission electron microscopy (HR-TEM) analysis. FE-SEM investigations were carried out using a JEOL (JSM-6340F) instrument. The HR-TEM studies were carried out for PAM and APM-200 samples by using a JEOL JEM-ARM200F instrument operated at 200 kV (point resolution = 0.11 nm) at the Research Laboratory for High Voltage Electron Microscopy, Kyushu University, Japan, to investigate the microstructure as well as presence of Ag at atomic scale in perovskite structure. The sample was dispersed in ethanol and treated in ultrasound for 10 min. A drop of very dilute suspension was placed on a holey-carbon-coated copper grid and allowed to dry by evaporation at ambient temperature. EDX analysis was also performed for PAM and APM-200 samples by using a JEOL TEM-EDX analyzer.

X-ray photoelectron spectra (XPS) were acquired using a KRATOS AXIS-165 spectrometer, Shimadzu Co. Ltd., operating at a pressure of $\approx 10^{-9}$ Torr, at room temperature with an Al $K\alpha$ monochromator source (photon energy = 1486.6 eV). The overall instrumental resolution was ≈0.3 eV. Pass energy for survey scan and core level spectra were kept at 80 and 40 eV, respectively. Charging effects were corrected by adjusting the binding energy of the C 1s peak to 285.0 eV. The binding energy values of the observed elements are compared with standard reference data from the National Institute of Standards and Technology (NIST). Peak areas were estimated by integrating the appropriate signals after data analysis.

O_2-TPD and H_2-TPR analyses were performed in a BEL-CAT instrument (BEL Japan), equipped with a TCD detector. A fixed bed of granules of catalyst was placed in a quartz tube and prior to each temperature-programmed oxygen desorption (TPD) run, the catalyst was heated to 800 °C (APM-550 and APM-200 samples were preheated at 500 and 200 °C, respectively) under an air flow of 30 mL/min. After 30 min of isothermal heating at this temperature, the sample was cooled to 40 °C under the same air flow. Afterward, helium was fed to the reactor at the low rate of 10 mL/min, and helium was kept flowing for 30 min at room temperature to purge any excess air. The catalyst was then heated to 800 °C at a constant heating rate of 10 °C/min under the same helium flow, and O_2 desorbed during the heating was analyzed using the thermal conductivity detector (TCD). For H_2-TPR experiments, the catalyst was pretreated under a flow of helium (30 mL/min) at 500 °C (APM-200 sample was preheated at 200 °C) for 30 min and cooled to 40 °C under the same flow. The reduction of catalyst was followed by heating the catalyst to 800 °C at a constant heating rate of 10 °C/min under the 5% H_2−N_2 flow, and consumption of H_2 during the heating was determined by using a TCD.

Catalytic Activity Test. The catalytic activity of all the synthesized catalysts was investigated for CO and soot oxidation reactions. The catalytic CO oxidation was carried out in a fixed bed, steady state type gas reactor as depicted in Figure S1 (Supporting Information). Granules of catalysts (0.1 g) were packed in a quartz reactor for catalytic run, and the temperature of the reactor was maintained by using a PID controlled furnace. Prior to the catalytic activity test, the catalysts were pretreated at 400 °C (APM-200 sample was preheated at 200 °C) for 1 h in a flow of helium for surface cleaning. The total flow rate of 100 cm^3/min of high-purity gases (0.5% CO balance He and 5% O_2; W/F = 0.06 g s/mL) was measured by mass flow controllers (Horiba, Japan). After the catalyst had attained steady state over a period of 30 min at each temperature, the effluent gas was analyzed for CO and CO_2 by a gas chromatograph (Shimadzu GC-8A) using a molecular sieve 5A column as well as a Porapak column.

The catalytic activity was expressed in terms of conversion (X) of CO gas according to the following equation:

$$X_{CO} = (P_{CO\,in} - P_{CO\,out})/P_{CO\,in}$$

The catalytic soot oxidation was studied by thermogravimetric analysis on a Rigaku-TAS-200 instrument and using commercially available carbon black (Sigma-Aldrich) as a substitute for soot. For oxidizing carbon black, the mixture of carbon black and catalysts was heated at 5 °C/min from 30 to 700 °C in an air atmosphere. The catalyst and carbon black weight ratio used was around 95:5, and the experiments were performed by following both tight and loose contact conditions. In tight contact, the mixture of catalyst and carbon was ground in a mortar and pestle for about 5 min, whereas the catalyst and carbon were physically mixed by spatula in a loose contact method. The blank TG experiments were also performed with only catalyst samples to account for any weight loss due to water desorption, etc.

RESULTS AND DISCUSSION

The XRD patterns for bare (PM), silver-substituted (PAM), and silver-dispersed (APM-550 and APM-200) perovskite catalysts are shown in Figure 1. All four X-ray diffraction

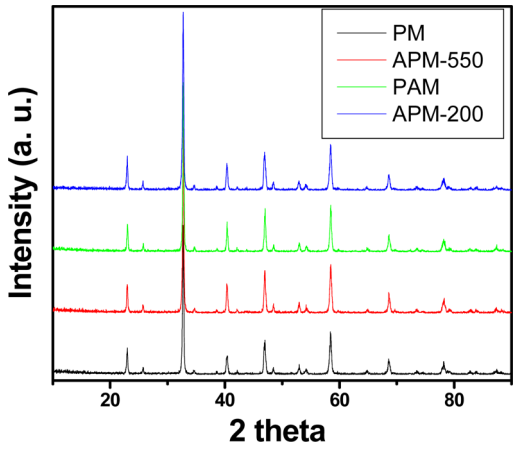

Figure 1. XRD patterns for $PrMnO_{3+\delta}$ (PM), 1 wt % Ag/$PrMnO_{3+\delta}$-550 (APM-550), $Pr_{0.9775}Ag_{0.0225}MnO_{3+\delta}$ (PAM), and 1 wt % Ag/$PrMnO_{3+\delta}$-200 (APM-200).

patterns were compared with the standard JCPDS database, which confirms the formation of crystalline orthorhombic phase (*Pbnm* space group) with perovskite structure (JCPDS 08-0354). It was not possible to identify the presence of separate Ag species such as Ag metal or Ag_2O in the surface-dispersed or Ag-substituted catalysts by means of XRD, mainly due to the lower amount and high dispersion of Ag. The lattice parameters (a, b, c) were calculated to investigate the effect of Ag on perovskite by dispersion as well as substitution. As shown in Table S1 (Supporting Information), similar cell parameters were obtained for all four samples, thereby confirming no significant change in unit cell dimension even if a small amount of Ag is incorporated in the lattice.

FE-SEM photographs of catalytic materials are shown in Figure S2 (Supporting Information). All of the materials show

dx.doi.org/10.1021/cs500880w | ACS Catal. 2015, 5, 301−309

somewhat porous morphology, which is because of the use of the citrate synthesis method. The rapid combustion of citrate in the spongy precursor during synthesis leads to porous morphology as reported earlier.[26] However, no significant morphological changes were observed in FE-SEM images for Ag-dispersed/substituted PM samples, which could be due to the low amount of Ag loading. Figures S3 and S4 show EDX compositional analysis for PAM and APM-200 samples, respectively, which confirms the presence of Pr, Ag, and Mn in both samples. The PAM and APM-200 samples were further analyzed by HR-TEM as shown in Figures S5 and S6, respectively. The TEM images reveal the particle size in nanoscale range, that is, ≈50−100 nm. For APM-200 sample, HR-TEM images show the presence of silver oxide nanoparticles of around 10 nm size, as shown in Figure S6. HR-TEM images also confirm the highly ordered crystalline structure for both PAM and APM-200 perovskite samples. The HAADF-STEM image of PAM and the corresponding EDX line profile of Pr and Ag are shown in Figure 2 and also in

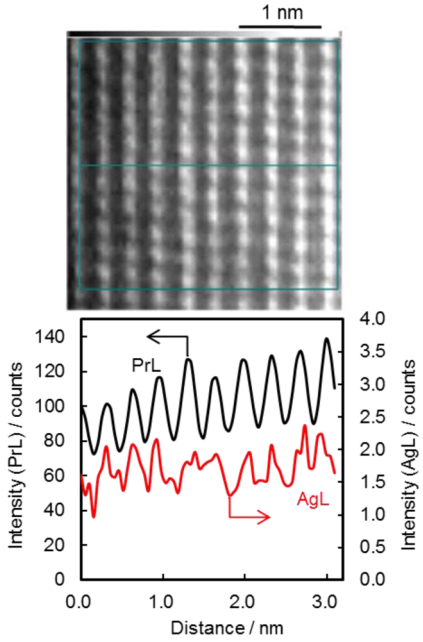

Figure 2. HAADF-STEM image and EDX line profiles of Pr and Ag of $Pr_{0.9775}Ag_{0.0225}MnO_{3+\delta}$ (PAM).

Figure S7. The presence of Pr in the row representing the A-site of ABO_3 type perovskite structure was clearly observed. The intensity of the AgL line was quite weak and less resolved as compared to that of Pr, because of its low concentration, but interestingly the distribution of Ag was synchronized with that of Pr on the same position. This is unambiguous evidence that Pr and Ag are present in the same atomic column or crystallographic position for the PAM sample, which confirms the partial substitution of Pr by Ag. For APM-200, no evidence of the presence of Ag in the column of Pr atoms was observed, whereas incorporation of Ag in the lattice was not completely excluded for APM-550. Thus, the present data can be considered as direct evidence for the presence of Ag along with Pr at the A site of ABO_3 perovskite composition.

XPS survey spectra (Figure S8, Supporting Information) for PM show sharp peaks of Pr, Mn, C, and O, whereas those for APM-550, PAM and APM-200 show the presence of Ag at 367.7−368.4 eV.[25] The binding energy (BE) values and doublet separation (ΔE) of Ag 3d and Mn 2p levels are presented in Table S2, and these results are in good agreement with standard values.[27] Detailed analysis of core level spectra of Pr, Ag, Mn, and O showed that Pr existed only in the +3 oxidation state in all samples (Figure S9), whereas existing states of Mn and Ag are different among different samples. Figure S10 shows the deconvoluted XPS Mn core level spectra in the BE range 639−659 eV, obtained for PM and Ag-substituted/dispersed samples. Deconvoluted XPS oxygen core level spectra show different oxygen species for all of the samples as shown in Figure S11, and the related detailed discussion is given in the Supporting Information. Deconvoluting the peaks into Gaussian components using appropriate positions and fwhm shows that Mn exists in both Mn^{3+} (642.12, 653.58 eV) and Mn^{4+} (643.44, 655.00 eV) oxidation states in PM. In addition, characteristic shakeup satellite peaks were observed at 645.37 and 656.85 eV, respectively. Quantitative analysis of deconvoluted peaks shows the composition of Mn^{3+}/Mn^{4+} to be 79%/21% in the PM sample (Table S3). The presence of Mn^{4+} means that PM has an oxidative nonstoichiometry ($PrMnO_{3+\delta}$) as in the case of $LaMnO_{3+\delta}$, in which Jahn−Teller distortion of Mn^{3+} is mitigated by the partial introduction of Mn^{4+}.[8] Provided that the surface Mn^{3+}/Mn^{4+} composition estimated from XPS results is representative of the bulk compopsition, δ in $PrMnO_{3+\delta}$ can be calculated to be 0.105, which is reasonably close to the reported values for $LaMnO_{3+\delta}$ ($\delta \approx 0.12$). The Mn^{3+}/Mn^{4+} ratio in APM-200 was practically the same as that observed for PM, because Ag is not incorporated in the bulk of PM, as stated above. For PAM, the average oxidation state of Mn (Mn^{3+}/Mn^{4+} = 74.1%/25.9%) is incresaed as compared with that in PM. This suggests incorporation of Ag in the perovskite structure, that is, the partial substitution of Ag^+ for Pr^{3+} while keeping the oxidative nonstoichiometry of perovskite ($Pr_{0.9775}Ag_{0.0225}MnO_{3.107}$). Oxidative nonstoichiometry values were corroborated by H_2-TPR quantification analysis (Supporting Information). A slight change was observed in the Mn^{3+}/Mn^{4+} ratio for the APM-550 sample, which suggests that a part of Ag is substituted in the perovskite lattice structure. This could be due to the high calcination temperature (550 °C) for Ag impregnation, which facilitates the partial introduction of Ag into the lattice.

Distinct Ag peaks of XPS Ag 3d core level spectra were observed for PAM, APM-550, and APM-200, respectively, as shown in Figure 3. Assignment of the oxidation state of Ag is quite complicated because Ag is one of the elements with negative BE shift with increase in oxidation number. The BE shift between 0 and +1 is relatively small, and the BE value is dependent on particle size.[27−29] The general criterion of discrimination is that Ag^0 and Ag^+ give a $3d_{5/2}$ peak above and below 368 eV, respectively. The weak Ag $3d_{5/2}$ peak was observed at 367.79 eV for PAM, indicating that Ag is in +1 state. For the APM-200 sample, in which the presence of bulk Ag_2O was confirmed by TEM (Figure S6, Supporting Information) as well as O_2-TPD and H_2-TPR (vide infra), the broad peak at 368.35 eV suggests the presence of both Ag^+ and Ag^0. The Ag $3d_{5/2}$ peak was observed at 367.84 eV for APM-550 in which the presence of both surface-dispersed Ag metal and Ag^+ substituted in the perovskite lattice was suggested by other methods. The intensity of the observed Ag peak increases in the order PAM < APM-550 < APM-200, which clearly indicates the higher surface concentration of Ag/Ag_2O for Ag-dispersed samples than for Ag-substituted samples.

dx.doi.org/10.1021/cs500880w | ACS Catal. 2015, 5, 301−309

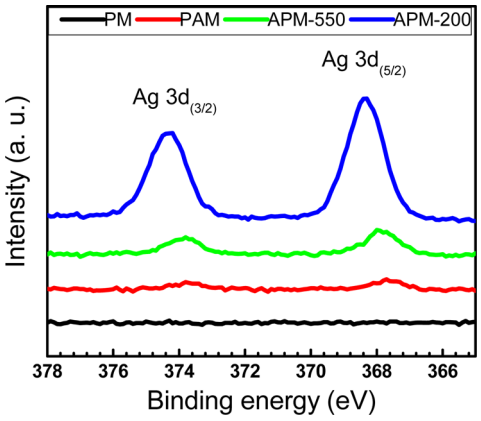

Figure 3. XPS Ag 3d core level spectra for $PrMnO_{3+\delta}$ (PM), 1 wt % $Ag/PrMnO_{3+\delta}$-550 (APM-550), $Pr_{0.9775}Ag_{0.0225}MnO_{3+\delta}$ (PAM), and 1 wt % $Ag/PrMnO_{3+\delta}$-200 (APM-200).

O_2-TPD profiles for all four catalysts are shown in Figure 4a. A two-peak desorption profile was observed for all samples, and

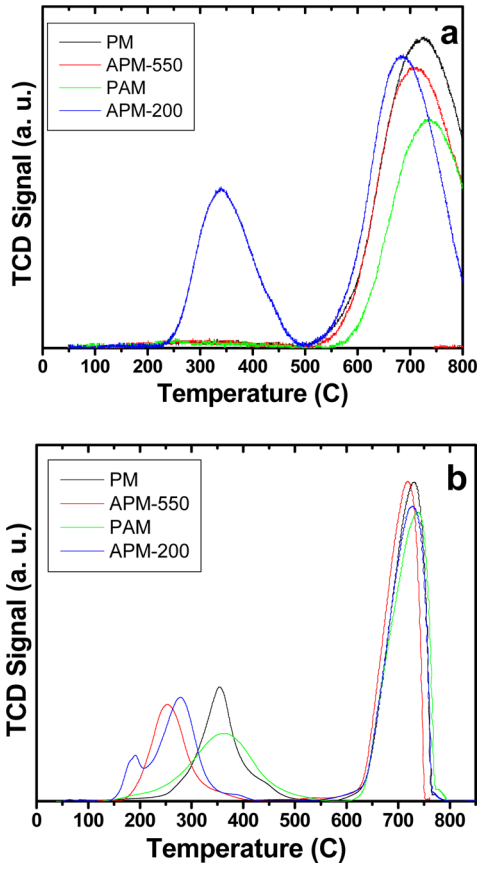

Figure 4. O_2-TPD (a) and H_2-TPR (b) profiles for $PrMnO_{3+\delta}$ (PM), 1 wt % $Ag/PrMnO_{3+\delta}$-550 (APM-550), $Pr_{0.9775}Ag_{0.0225}MnO_{3+\delta}$ (PAM), and 1 wt % $Ag/PrMnO_{3+\delta}$-200 (APM-200).

oxygen desorption was qualitatively determined by means of mass spectroscopy. In the low-temperature region, a significant desorption peak (≈200−480 °C) was observed for APM-200 catalyst, which corresponds to oxygen desorption by the decomposition of surface silver oxide to silver metal. For PM, PAM, and APM-550 samples, a low-temperature peak with quite low intensity was observed at the temperature range ≈200−390 °C, which corresponds to desorption of surface-adsorbed oxygen. The absence of the distinct desorption peak for PAM indicates that the Ag^+ state is stabilized by incorporation in the perovskite lattice, and that for APM-550 is due to the fact that Ag is present as stabilized Ag^+ in perovskite and Ag^0 dispersed on the surface. The second high temperature desorption peak of PM is due to the release of oxygen-excess nonstoichiometry as reported for $LaMnO_{3+\delta}$.[8,30] It should be noted that Mn^{4+} introduced as a result of charge compensation is hardly reduced in this temperature range.[8,30] In the case of APM-200, the lattice oxygen desorption peak is shifted to lower temperature as compared to PM. This could be due to the presence of surface Ag^0 formed by the decomposition of Ag_2O in the low-temperature peak, which may facilitate Mn^{4+} reduction through mediation of oxygen association reaction at the surface, $2O^{2-} \rightarrow O_2$. In PAM, the Mn^{4+} state is more stable due to the presence of Ag^+ ions in the lattice (charge compensation).[8,31] Accordingly, the lattice oxygen desorption peak is shifted to higher temperature and the desorption amount decreases in this compound. In the case of APM-550, the peak temperature and the amount of the lattice desorption were between those of APM-200 and PAM, because of the presence of Ag^+ in perovskite as well as Ag^0 dispersed on the surface. TPD results thus nicely corroborate with the state of Ag as observed from HR-TEM and XPS studies.

H_2-TPR profiles for PM, PAM, APM-550, and APM-200 samples are shown in Figure 4b. Two major reduction peaks were observed for PM, PAM, and APM-550. The quantitative discussion of H_2 consumption and the reduction reactions occurring under low- and high-temperature regions are given in the Supporting Information (Table S4). Focusing on the reduction behavior of Mn ions, all of the Mn^{4+} ions are reduced to Mn^{3+} and a part of Mn^{3+} is reduced to Mn^{2+} under the low-temperature peak, whereas the remaining Mn^{3+} ions are reduced to Mn^{2+} under the high-temperature peak. The low-temperature peaks, which involve the catalytically important reduction of Mn^{4+} to Mn^{3+} and, if any, Ag^+ to Ag^0, deserve discussion here. As compared to Ag-free PM, the low-temperature reduction was promoted by the presence of surface-dispersed Ag species (APM-200, 550), whereas the substituted Ag ion showed little effect on the reduction behavior. In the case of APM-200, the first low-temperature shoulder peak around 200 °C was possibly due to the reduction of Ag_2O to metallic Ag, and the Ag metal thus formed facilitates the reduction of PM with higher H_2 activation ability than the bare oxide surface, due to the spillover effect of metallic Ag. In the case of APM-550, most of the silver is present as Ag metal and, therefore, the TPR peak around 200 °C was not observed. However, for the same spillover effect, the reduction phenomenon of Mn ions was observed at relatively lower temperature than that for PM. For PAM, such an effect was not observed not only because of the enhanced stability of substituted Ag^+ in perovskite as compared with Ag^+ in Ag_2O but also due to the lesser amount of Ag metal, which is formed by the reduction of Ag^+ in perovskite successively from the surface to the inner part of perovskite particles. These TPR results hence further substantiate the altered redox properties of perovskite by means of Ag dispersion and substitution achieved in different samples, as also corroborated by XPS and TPD findings. In this way, HR-TEM, XPS, O_2-TPD, and H_2-TPR investigations unambiguously substantiate that the Ag is present as oxide on the surface of APM-200 and as metallic silver on the

dx.doi.org/10.1021/cs500880w | ACS Catal. 2015, 5, 301−309

surface with some amount present in the lattice for APM-550, whereas Ag is present as substituted at A site of ABO_3 structure in the lattice for PAM catalyst.

The catalytic activity results for PM, PAM, APM-550, and APM-200 materials for CO oxidation reaction are given in Figure 5. The CO conversion at a given temperature of 200 °C,

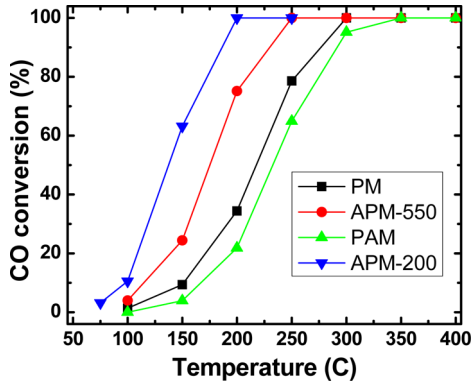

Figure 5. CO oxidation as a function of temperature for $PrMnO_{3+\delta}$ (PM), 1 wt % $Ag/PrMnO_{3+\delta}$-550 (APM-550), $Pr_{0.9775}Ag_{0.0225}MnO_{3+\delta}$ (PAM), and 1 wt % $Ag/PrMnO_{3+\delta}$-200 (APM-200) catalysts (feed, 0.5% CO + 5% O_2, balance He; SV ≈ 90000 h^{-1}).

for example, increased as PAM < PM < APM-550 < APM-200, suggesting that dispersed and substituted Ag species enhance and deteriorate the CO oxidation activity, respectively. To eliminate the difference of specific surface area (S_{BET}), the rate constant per S_{BET} was calculated by assuming the pseudo-first-order reaction to CO concentration. As shown in Table S5 (Supporting Information), intrinsic activity per S_{BET} for CO oxidation increased as PAM < PM < APM-550 < APM-200. This corroborates that Ag species dispersed on the surface and incorporated in perovskite lattice respectively enhance and deteriorate the activity of PM catalyst. As expected from TPD results, the redox change of Ag_2O dispersed on the surface occurs easily. This should be why APM-200 shows better activity. On the contrary, Ag^+ substituted in the perovskite lattice is stabilized, so that it no longer works as an active site with facile redox property. Furthermore, the Mn^{4+} state is stabilized when it is formed as a result of charge compensation of Ag^+ substitution for Pr^{3+}. The decrease in the activity of PAM as compared with PM might be caused by the double deterioration of facile redox property of Ag^+ and Mn^{4+}. The apparent activation energy for CO oxidation (E_a) for all of the catalysts was calculated using an Arrhenius plot as depicted in the Supporting Information (Figure S12). As given in Table S5 (Supporting Information) the E_a value decreases in the order PAM > PM ≈ APM-550 > APM-200. The discussion of E_a should be based on the reaction mechanism, but the lowest and highest E_a values must be related to the enhanced redox property of APM-200 due to the presence of Ag_2O and the retarded redox property of PAM due to the substitution of Ag^+, respectively. There are various reaction mechanisms proposed for the catalytic CO oxidation, which mainly depend on the metal active site, supports, oxides, and composition of the catalyst used as well as reaction conditions.[32] The CO oxidation over perovskite oxide-based materials involves either the Langmuir–Hinshelwood (L-H) mechanism or the Mars–van Krevelen (MvK) pathway or a combination of L-H and MvK mechanisms depending on the active site, reaction temperature, and redox properties as well as catalytic composition used, as reported by numerous researchers.[11,32−35] It is commonly accepted that the L-H mechanism is based on suprafacial gas-phase reaction, which involves only the surface active/vacant/metal site. While the MvK mechanism is based on the participation of surface oxygen and/or lattice/bulk oxygen from the catalyst over reduction−oxidation reactions. On the basis of extensive literature reports and the present results, we propose that on bare perovskite, the CO oxidation reaction may preferably take place by following the L-H mechanism. However, CO oxidation may follow a combination of L-H and MvK mechanisms over Ag-dispersed perovskite samples due to the presence of active Ag/Ag_2O redox couple on the perovskite surface as explained with O_2-TPD and H_2-TPR interpretations of present catalysts. Such studies on other perovskite compositions would further add to this understanding.

Soot oxidation experiments were also performed on bare soot as well as with all of the catalytic materials by following the tight as well as loose contact method, and the results are given in Figure 6 as well as Figure S13 and Tables S6 and S7

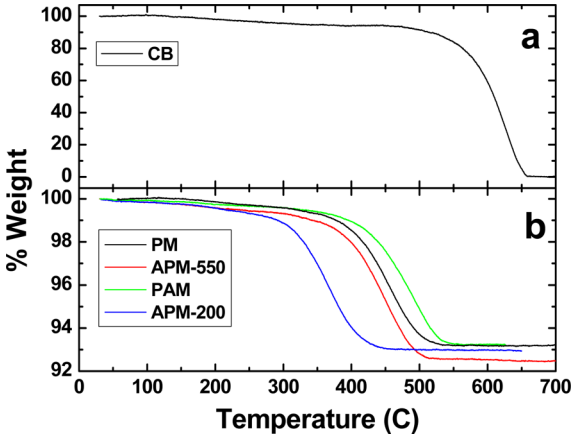

Figure 6. Thermogravimetric analysis (TG) results: (a) carbon black (CB) oxidation; (b) $PrMnO_{3+\delta}$ + CB (PM), 1 wt % $Ag/PrMnO_{3+\delta}$-550 + CB (APM-550), $Pr_{0.9775}Ag_{0.0225}MnO_{3+\delta}$ + CB (PAM) and 1 wt % $Ag/PrMnO_{3+\delta}$-200 + CB (APM-200) oxidation under tight contact condition.

(Supporting Information). The oxidation of bare soot started at around 492 °C and was completed at 659 °C under the present condition (Figure 6a and Figure S13 in the Supporting Information). This combustion was significantly improved; that is, the combustion temperature was shifted to lower temperature, when Pr–Mn-based perovskite catalyst was mixed with the soot. A similar trend was observed for soot oxidation activity as observed in the case of CO oxidation reaction for these catalysts. The soot oxidation activity increases in the order PAM < PM < APM-550 < APM-200.

Soot Oxidation under Tight Contact Condition. PM catalyst shows the initial soot combustion around 315 °C, whereas completion of combustion was achieved at 531 °C, which is 128 °C lower than for noncatalyzed soot oxidation. The very significant soot oxidation activity of PM was further improved by surface Ag/Ag_2O dispersion. APM-550 shows T_i at 315 °C and T_f at 516 °C, which are 143 and 15 °C lower than for noncatalyzed and PM-catalyzed oxidation, respectively. APM-200 catalyst shows T_i at 247 °C and T_f at 453 °C, which are 206 and 78 °C lower than for noncatalyzed and PM-

dx.doi.org/10.1021/cs500880w | ACS Catal. 2015, 5, 301−309

catalyzed oxidation, respectively. APM-550 and APM-200 thus show even further improved catalytic activity than bare PM, thereby implying the promotional effect of surface-dispersed Ag/Ag_2O. Especially, APM-200 shows better soot oxidation activity even as compared to APM-550 catalyst, which could be due to the highly active surface Ag_2O sites of APM-200. As already discussed, some of the Ag is present as partially substituted and stabilized in perovskite structure of APM-550 catalyst, which in turn reduces the number of active Ag sites on the surface of this catalyst.

Soot Oxidation under Loose Contact Condition. As expected, the soot oxidation activity under loose contact condition is slightly inferior to that under tight contact for all catalysts, as shown in Figure S13 and Table S7 (Supporting Information). PM catalyst shows the initial soot combustion around 460 °C, whereas completion of combustion was achieved at 634 °C, which is 25 °C lower than for noncatalyzed soot oxidation. APM-550 shows T_i at 435 °C, and T_f at 630 °C. The T_f is 29 °C lower than for noncatalyzed oxidation. APM-200 catalyst shows T_i at around 320 °C, and T_f at 610 °C. The T_f is 49 °C lower than for noncatalyzed oxidation. This noticeable decrease in soot oxidation activity under loose contact as compared to tight contact condition is because of relatively less homogeneity, that is, poor contact between soot and catalyst in this peculiar catalytic reaction in which catalyst and one of the reactants (soot) both are in solid phase. Nonetheless, the soot oxidation activity of the APM-200 sample under loose contact condition also can be considered as excellent and quite comparable to that of tight contact, because the initial soot combustion temperature was similar in both contact conditions.

There are quite a few reaction mechanisms proposed for soot oxidation, including electron transfer, triple-point contact, surface redox, spillover, combination of surface redox and spillover, and redox mechanism by lattice oxygen.[36−41] Soot oxidation over perovskite type oxides involves either surface redox via weakly chemisorbed oxygen (suprafacial) or redox mechanism via lattice oxygen.[37,38] It is quite difficult to discriminate the plausible mechanism involving either surface oxygen ions or lattice oxygen. Fino et al. proposed that the soot oxidation over chromite-based perovskites takes place via weakly chemisorbed suprafacial oxygen.[38] In contrast, they also reported that in the case of Co-based perovskites, the lattice oxygen plays a major role for soot oxidation.[37] Soot oxidation on Mn-based perovskite also follows a mechanism similar to the Co system, where the soot oxidation takes place via readily reducible lattice oxygen, following the MvK mechanism.[42] These readily reducible lattice oxygen species are believed to be mobile, which can migrate from the lattice to the surface followed by simultaneous reoxidation of the lattice through gas phase oxygen. Hence, it is very clear that the soot oxidation pathway on perovskite catalysts mainly depends on their composition as well as redox properties. On the basis of the literature and detailed redox property studies via O_2-TPD and H_2-TPR, it is quite possible that the soot oxidation on the present catalysts could take place via the MvK mechanism. In the case of Ag-dispersed catalysts, the Ag/Ag_2O redox couple also plays a major role for oxidation reaction and facilitates the reducibility of Mn ions.[43,44] This synergistic effect was clearly substantiated by XPS, O_2-TPD, and H_2-TPR studies and governs the improved soot oxidation on such catalysts.

Stability Studies and Post-mortem Analysis. It is generally accepted that the perovskite-based oxides are thermally stable materials even under quite harsh reaction conditions. However, we have performed stability tests for both silver-substituted (PAM) and -dispersed (APM-200) catalysts after CO as well as soot oxidation reactions. The CO exposure/oxidation was carried out for 24 h with gas feed containing 0.5% CO and 5% O_2 with the balance He (W/F = 0.06 g s/mL) at 200 °C (APM-200) and 400 °C (PAM). Practically no change was observed in CO oxidation activity for both catalysts even after 24 h of exposure under this quite high concentration of CO in the feed. For both APM-200 and PAM catalysts, soot oxidation was also carried out under tight contact condition at 700 °C for 2 h in a muffle furnace, and the same used catalyst was reused for three consecutive cycles. These are relatively much more severe conditions than those followed for the soot oxidation reaction using a TG machine. Once again, there was no change in catalytic activity. The present perovskite catalysts therefore show stable catalytic activity under these conditions of multicycle performance. Following the CO and soot exposure for a prolonged time, the structure and redox properties of samples were again characterized by XRD, O_2-TPD, and H_2-TPR, and the results are shown in the Supporting Information (Figure S14).

XRD. The XRD patterns for both CO- and soot-exposed catalysts are shown in Figure S14a,b. The XRD analysis confirms the intact perovskite structure for both APM-200 and PAM samples even after exposure to CO and multiple-cycle soot oxidation, thus implying their structural stability. Not much can be said about the stability of silver by these XRD results as the presence of silver was not identified even in fresh samples, due to its low concentration and high dispersion.

O_2-TPD. O_2-TPD profiles for both CO- and soot-exposed catalysts are depicted in Figure S14c,d. The observed TPD profiles of CO-exposed APM-200 and PAM catalysts are exactly the same as those obtained for respective fresh catalysts, which confirms the unaffected oxygen desorption properties in the used catalysts. A significant low-temperature desorption peak of CO-exposed APM-200 sample also clearly implied the presence of Ag as oxide on the surface of perovskite structure. In the case of soot-exposed catalysts, no significant change was observed in the TPD profile of PAM catalyst, thus showing its stable redox properties. However, the amount of low-temperature desorption was decreased for exposed APM-200 samples, whereas the desorption temperature is also shifted toward higher temperature for soot-exposed sample. This could be due to high-temperature soot oxidation experiment leading to reduction of silver oxide to Ag as well as partial migration of Ag into the perovskite lattice. It should be noted that this sample was originally synthesized by heating at only 200 °C after silver incorporation and thus expected to show such changes after high-temperature exposure.

H_2-TPR. The H_2-TPR profiles for CO-exposed APM-200 and PAM catalysts are shown in Figure S14e,f. As observed in TPD profiles, the TPR profiles of CO-exposed catalysts are also similar to those obtained for fresh samples. From these TPR profiles, we could conclude that Ag remains as oxide on the surface and substituted as Ag ion even after 24 h of exposure of 0.5% CO on APM-200 and PAM catalysts. The redox behaviors of these catalysts are therefore stable under the CO oxidation reaction conditions used. As depicted in Figure S14e, the TPR profile of soot-exposed APM-200 shows some difference as compared to the fresh catalyst, and the low-temperature reduction peak was shifted toward higher temperature. As already mentioned, this difference could be due to the high-

dx.doi.org/10.1021/cs500880w | ACS Catal. 2015, 5, 301−309

temperature exposure during the soot oxidation experiment for this sample originally synthesized at 200 °C. In the case of the TPR profile of soot-exposed PAM catalyst, no significant effect was observed as compared to the fresh catalyst.

CONCLUSION

A systematic attempt has been made to study the physicochemical, structural, and catalytic properties of $PrMnO_{3+\delta}$ type perovskite compositions containing small amounts of Ag dispersed/substituted in the ABO_3 structure. The presence and effects of Ag as partially substituted in lattice as well as dispersed on the surface of perovskite were studied in detail by using several techniques. It was possible to establish the presence of Ag along with Pr at the A position of perovskite structure in the PAM catalyst by using direct evidence of TEM atomic level elemental mapping and to correlate its influence on perovskite properties. In the case of APM-550, some of the silver was observed to be partially substituted in the lattice structure, which is because of reasonably high temperatures used after Ag impregnation on the PM surface, as observed through XPS and O_2-TPD results. In this way, Ag was observed to be present on the surface as well as in the perovskite lattice for this APM-550 catalyst, which implies the mobility of Ag as a function of synthesis temperature. Only surface Ag_2O phase was observed for APM-200 sample, which was confirmed by TEM images, and corroborated by XPS, TPD and TPR studies. These materials were studied for their CO and soot oxidation activity. The APM-200 catalyst shows better activity than other bare and Ag-doped perovskite catalysts for both CO and soot oxidation reactions. This is mainly because of the fact that silver oxide nanoparticles on the catalyst surface with facile redox property serve as catalytically active sites. It is found that Ag remains as Ag_2O on the surface of APM-200 even after low-temperature CO oxidation due to prevailing oxidative conditions during CO oxidation reaction. The Ag species incorporated in the perovskite lattice is too stabilized to work as an active site, and therefore no significant increase in activity was observed. Ag appears to be stable in substituted perovskite, as concluded by post-mortem studies on used catalysts. It is therefore possible to convincingly follow the presence of Ag and its impacts on perovskite structure, as Ag is being explored as a potential promoter metal for catalytic activity of perovskite and other catalyst compositions for a variety of reactions.

ASSOCIATED CONTENT

Supporting Information

The following file is available free of charge on the ACS Publications website at DOI: 10.1021/cs500880w

Schematic of the fixed bed catalyst evaluation system, SEM photographs, EDX patterns, TEM photographs, XPS survey scan spectra, XPS deconvoluted spectra for Pr 4d, Mn 2p, and O 1s core level spectra, Arrhenius plot for CO oxidation, TG results, and post-mortem analysis (Figures S1−S14); structural and physical properties of catalysts, XPS binding energy results, XPS quantitative results, H_2-TPR data, rate constants (k_w, k_s), apparent activation energy (E_a) data, and TG results (Tables S1−S7); H_2-TPR data and discussion (PDF)

AUTHOR INFORMATION

Corresponding Author

*(N.L.) E-mail: nk_labhsetwar@neeri.res.in.

Notes

The authors declare no competing financial interest.

ACKNOWLEDGMENTS

We dedicate this work to the late Professor Y. Teraoka (one of the authors of this paper who suddenly passed away on August 3, 2014) for his outstanding contributions in the field of catalysis and perovskites. S.K.M. acknowledges the Council of Scientific and Industrial Research (CSIR) for providing financial support (Senior Research Fellowship). We are grateful to Takeshi Daio of Kyushu University for excellent TEM images and data. We thank Rohini Khobragade and Pallavi Mungse (CSIR-NEERI) as well as A. Tou and T. Uchiyama (Kyushu University) for their contributions in other characterization studies. This work was carried out under the DST-JSPS bilateral project (Project GAP1962) between CSIR-NEERI, India, and Kyushu University, Japan.

REFERENCES

(1) Huang, Y. H.; Dass, R. I.; Xing, Z. L.; Goodenough, J. B. *Science* **2006**, *312*, 254−257.
(2) Egilmez, M.; Chow, K. H.; Jung, J. A. *Mod. Phys. Lett.* **2011**, *B 25*, 697−722.
(3) Sunarso, J.; Baumann, S.; Serra, J. M.; Meulenberg, W. A.; Liu, S.; Lin, Y. S.; Diniz da Costa, J. C. *J. Member. Sci.* **2008**, *320*, 13−41.
(4) Chroneos, A.; Vovk, R. V.; Goulatis, I. L.; Goulatis, L. I. *J. Alloys Compd.* **2010**, *494*, 190−195.
(5) Ebbinghaus, S. G.; Abicht, H.; Dronskowski, R.; Muller, T.; Reller, A.; Weidenkaff, A. *Prog. Solid State Chem.* **2009**, *37*, 173−205.
(6) Fine, G. F.; Cavanagh, L. M.; Afonja, A.; Binions, R. *Sensors* **2010**, *10*, 5469−5502.
(7) Zhu, J.; Thomas, A. *Applied Catal. B: Environ.* **2009**, *92*, 225−233.
(8) Yamazoe, N.; Teraoka, Y. *Catal. Today* **1990**, *8*, 175−199.
(9) Tejuca, L. G.; Fierro, J. L.; Tascon, J. M. D. *Adv. Catal.* **1989**, *36*, 237−328.
(10) Swamy, C. S.; Cristopher, J. *Catal. Rev. Sci. Eng.* **1992**, *34*, 409−425.
(11) Pena, M. A.; Fierro, J. L. G. *Chem. Rev.* **2001**, *101*, 1981−2017.
(12) Tou, A.; Einaga, H.; Teraoka, Y. *Catal. Today* **2013**, *201*, 103−108.
(13) Zhou, K.; Chen, H.; Tian, Q.; Hao, Z.; Shen, D.; Xu, X. *J. Mol. Catal. A: Chem.* **2002**, *189*, 225−232.
(14) Eyssler, A.; Winkler, A.; Mandaliev, P.; Hug, P.; Weidenkaff, A.; Ferri, D. *Appl. Catal. B: Environ.* **2011**, *106*, 494−502.
(15) Cimino, S.; Casaletto, M. P.; Lisi, L.; Russo, G. *Appl. Catal. A: Gen.* **2007**, *327*, 238−246.
(16) Nishihata, Y.; Mizuki, J.; Akao, T.; Tanaka, H.; Uenishi, M.; Kimura, M.; Okamoto, T.; Hamada, N. *Nature* **2002**, *418*, 164−166.
(17) Tanaka, H.; Uenishi, M.; Taniguchi, M.; Tan, I.; Narita, K.; Kimura, M.; Kaneko, K.; Nishihata, Y.; Mizuki, J. *Catal. Today* **2006**, *117*, 321−328.
(18) Guo, X.; Meng, M.; Dai, F.; Li, Q.; Zhang, Z.; Jiang, Z.; Zhang, S.; Huang, Y. *Appl. Catal. B, Environ.* **2013**, *142*−*143*, 278−289.
(19) Wang, W.; Zhang, H.; Lin, G.; Xiong, Z. *Appl. Catal. B, Environ.* **2000**, *24*, 219−232.
(20) Liu, Z.; Hao, J.; Fu, L.; Zhu, T. *Appl. Catal. B: Environ.* **2003**, *44*, 355−370.
(21) Choudhary, V. R.; Uphade, B. S.; Pataskar, S. G. *Fuel* **1999**, *78*, 919−921.
(22) Kucharczyk, B.; Tylus, W. *Appl. Catal. A: Gen.* **2008**, *335*, 28−36.
(23) Buchneva, O.; Rossetti, I.; Biffi, C.; Allieta, M.; Kryukov, A.; Lebedeva, N. *Appl. Catal. A: Gen.* **2009**, *370*, 24−33.
(24) Buchneva, O.; Rossetti, I.; Oliva, C.; Scavini, M.; Cappelli, S.; Sironi, B.; Allieta, M.; Kryukov, A.; Forni, L. *J. Mater. Chem.* **2010**, *20*, 10021−10031.

(25) Pecchi, G.; Campos, C. M.; Jiliberto, M. G.; Delgado, E. J.; Fierro, J. L. G. *Appl. Catal. A: Gen.* **2009**, *371*, 78−84.
(26) Russo, N.; Mescia, D.; Fino, D.; Saracco, G.; Specchia, V. *Ind. Eng. Chem. Res.* **2007**, *46*, 4226−4231.
(27) http://srdata.nist.gov/xps/Default.aspx.
(28) Gaarenstroom, S. W.; Winograd, N. J. *Chem. Phys.* **1977**, *67*, 3500−3506.
(29) Ferraria, A. M.; Carapeto, A. P.; Botelho do Rego, A. M. *Vacuum* **2012**, *86*, 1988−1991.
(30) Teraoka, Y.; Yoshimatsu, M.; Yamazoe, N.; Seiyama, T. *Chem. Lett.* **1984**, *13*, 893−899.
(31) Kumar, S.; Teraoka, Y.; Joshi, A. G.; Rayalu, S.; Labhsetwar, N. *J. Mol. Catal. A: Chem.* **2011**, *348*, 42−54.
(32) Royer, S.; Duprez, D. *Chem. Catal. Chem.* **2011**, *3*, 24−65.
(33) Yang, W.; Zhang, R.; Chen, B.; Bion, N.; Duprez, D.; Royer, S. *J. Catal.* **2012**, *295*, 45−58.
(34) Ouyang, X.; Scott, L. S. *J. Catal.* **2010**, *273*, 83−91.
(35) Hueso, L. J.; Martínez-Martínez, D.; Caballero, A.; González-Elipe, R. A.; Munc, S. B.; Salmerón, M. *Catal. Commun.* **2009**, *10*, 1898−1902.
(36) Stanmore, R. B.; Brilhac, F. J.; Gilot, P. *Carbon* **2001**, *39*, 2247−2268.
(37) Russo, N.; Furfori, S.; Fino, D.; Saracco, G.; Specchia, V. *Appl. Catal. B: Environ.* **2008**, *83*, 85−95.
(38) Fino, D.; Russo, N.; Saracco, G.; Specchia, V. *J. Catal.* **2003**, *217*, 367−375.
(39) Mckee, D. W. *Carbon* **1987**, *25*, 587−588.
(40) Baumgarten, E.; Schuck, A. *Appl. Catal.* **1988**, *37*, 247−257.
(41) Teraoka, Y.; Nakano, K.; Shangguan, W.; Kagawa, S. *Catal. Today* **1996**, *27*, 107−113.
(42) Wang, X.; Zhang, Y.; Li, Q.; Wang, Z.; Zhang, Z. *Catal. Sci. Technol.* **2012**, *2*, 1822−1824.
(43) Hernández-Giménez, M. A.; Castelló, L. D.; Bueno-López, A. *Chem. Papers* **2014**, *68*, 1154−1168.
(44) Guilhaume, N.; Bassou, B.; Bergeret, G.; Bianchi, D.; Bosselet, F.; Desmartin-Chomel, A.; Jouguet, B.; Mirodatos, C. *Appl. Catal. B: Environ.* **2012**, *119*, 287−296.